Nanoscale Horizons

COMMUNICATION

Check for updates

Two dimensional $NbSe_2/Nb_2O_5$ metal–semiconductor heterostructure-based photoelectrochemical photodetector with fast response and high flexibility†

Xiang Xu,‡*[a] Chunhui Lu,‡[b] Ying Wang,[a] Xing Bai,[a] Zenghui Liu,[a] Ying Zhang[a] and Dengxin Hua[a]

Two dimensional (2D) metal-semiconductor heterostructures are promising for high-performance optoelectronic devices due to fast carrier separation and transportation. Considering the superior metallic characteristics accompanied by high electrical conductivity in $NbSe_2$, surface oxidation provides a facile way to form $NbSe_2/Nb_2O_5$ metal-semiconductor heterostructures. Herein, size-dependent $NbSe_2/Nb_2O_5$ nanosheets were achieved by a liquid phase exfoliation method and a gradient centrifugation strategy. These $NbSe_2/Nb_2O_5$ heterostructure-based photodetectors show high responsivity with 23.21 $\mu A\ W^{-1}$, fast response time of millisecond magnitude, and wide band detection ability in the UV-Vis region. It is noticeable that the photocurrent density is sensitive to the surface oxygen layer due to the oxygen-sensitized photoconduction mechanism. The flexible testing of the $NbSe_2/Nb_2O_5$ heterostructure-based PEC-type photodetectors exhibits high photodetection performance even after bending and twisting. Beyond that, the solid-state PEC-type $NbSe_2/Nb_2O_5$ photodetector also achieves relatively stable photodetection and high stability. This work promotes the application of 2D $NbSe_2/Nb_2O_5$ metal-semiconductor heterostructures in flexible optoelectronic devices.

New concepts

Considering the superior metallic characteristics accompanied by high electrical conductivity in $NbSe_2$, surface oxidation provides an efficient way to form $NbSe_2/Nb_2O_5$ metal-semiconductor heterostructures (MSHSs). We aim to explore the photodetection performance of the size-dependent $NbSe_2/Nb_2O_5$ MSHSs. In this work, we demonstrate that this $NbSe_2/Nb_2O_5$ based photoelectrochemical (PEC) photodetector shows high responsivity, fast response time of millisecond magnitude, and wide band detection ability in the UV-Vis region. Additionally, this $NbSe_2/Nb_2O_5$ exhibits high photodetection performance even after flexible testing. Furthermore, the solid-state PEC-type $NbSe_2/Nb_2O_5$ photodetector also achieves relatively stable photodetection. This work provides an opportunity to synthesize 2D metal-semiconductor heterostructures, which have great potential for designing high-performance PEC-type photodetector applications.

Introduction

Two dimensional (2D) transition metal dichalcogenides (TMDs) have been widely designed for high-performance flexible optoelectronic devices due to their unique physical, chemical, and mechanical properties.[1,2] Among them, semiconducting layered TMD materials especially, MoX_2 or WX_2 (X = S or Se), show a tunable band gap with layer number,[3] stronger

light-absorption compared with traditional Si and GaAs,[4] and high solar energy conversion beyond 10%.[5] Accordingly, 2D semiconducting layered TMDs have been widely investigated and applied in optoelectronic applications.[6,7] Besides, 2D TMD-based semiconductor–semiconductor and semiconductor-insulator heterostructures have also been widely studied in both theory and experiments, because these heterostructures show novel physical phenomena and great potential in photovoltaic, optoelectronic, and energy storage devices.[8–10] However, their optoelectronic performance is strongly hindered due to the poor electrode contact. Recently, theoretical calculations have demonstrated that 2D metal-semiconductor heterostructures (MSHSs) not only weaken the Fermi level pinning, but also modulate the Schottky barrier. Although some MSHSs are reported, most of the studies focus on graphene-based MSHSs due to the limited 2D metallic materials. With the advancement of current industrial applications, metallic TMDs have been successfully synthesized and widely reported. As members of the metallic TMDs, $TaSe_2$, $NbSe_2$, and TaS_2 are mainly investigated in superconductivity[11,12] and the charge density wave phenomenon.[13] These metallic TMDs show no band gap and high electrical conductivity,[14,15] and have a great potential for good electrode contact in a 2D semiconductor device. $NbSe_2$, a representative of metallic TMDs, becomes a

[a] School of Mechanical and Precision Instrument Engineering, Xi'an University of Technology, Xi'an 710048, China. E-mail: xxuxxiang@xaut.edu.cn;
Tel: +86 15529500771
[b] Institute of Photonics & Photon-Technology, School of Physics, Northwest University, Xi'an 710069, China

‡ Xiang Xu and Chunhui Lu contributed equally to this work.

type II superconductor under 7.2 K.[16] Moreover, the metallic nature endows outstanding electronic transport ability. As such, it is promising to be an electrical contact and connect with semiconductors, forming metal-semiconductor heterostructures (MSHSs).[17,18] The experimental realization of $NbSe_2$-based MSHSs has demonstrated a high carrier mobility and reduced contact resistance.[19,20] Even though a few MSHSs have great potential in integrated electronics, the large-area synthesis is still a great challenge.

Surface oxidation is an easy and efficient way to construct heterostructures and tailor the performance of optoelectronic devices.[21] A thin oxidation layer was introduced as $In_2O_3/InSe$[22] and WO_x/WSe_2,[23] which can adjust the band edge positions and improve the performance of the photodetector. Considering poor stability of $NbSe_2$, surface oxidation treatment is easy to form the $NbSe_2/Nb_2O_5$ heterostructure[24] as exposed to air. Nb_2O_5 shows strong stability in an aqueous medium, a band gap of 3.4 eV and high light absorption in the UV region.[25,26] The heterostructure constructed with metallic $NbSe_2$, serving as an electrode contact, exhibits a higher mobility and markedly improves the charge transfer efficiency in the mixed $NbSe_2/Nb_2O_5$ heterostructure. The formation of the $NbSe_2/Nb_2O_5$ heterostructure renders it a promising candidate for semiconductor electronic and photodetector applications. It is well known that the solvent-assisted exfoliation technique can not only obtain 2D $NbSe_2$ nanosheet dispersions but also introduce the surface oxidation by size-separation.[24,27–30] This provides an opportunity to design $NbSe_2/Nb_2O_5$ MSHS based photodetectors and investigate the photoelectric properties. Different from field effect transistor (FET)-based photodetectors, photoelectrochemical (PEC)-type photodetectors act as a new functional photodetection system to detect the conversion of light-electric signals.[31–35] There are some inherent advantages: (i) easy to adjust in terms of photoelectric performance by light intensity and bias voltage; (ii) simple and low-cost measurement procedure; (iii) close-knit electrical contact to the sample between the redox electrolyte and solid electrode; (iv) efficient perpendicular charge separation and transport pathways. In this context, $NbSe_2/Nb_2O_5$ MSHS is expected to be applied into PEC-type photodetectors, which has not been reported yet to the best of our knowledge.

Herein, $NbSe_2/Nb_2O_5$ metal-semiconductor heterostructures were achieved by a solvent-assisted exfoliation technique with a gradient centrifugation method, and were characterized by transmission electron microscopy (TEM), scanning electron microscopy (SEM), X-ray diffraction (XRD), X-ray photoelectron spectroscopy (XPS) and atomic force microscopy (AFM). The $NbSe_2/Nb_2O_5$ MSHS-based PEC-type photodetector shows high responsivity, fast response time and recovery time, and wide band detection. It is worth pointing out that the sensitivity of the photocurrent density to ambient conditions is due to the oxygen-sensitized photoconduction mechanism. Furthermore, the $NbSe_2/Nb_2O_5$ PEC-type photodetector still exhibits high photodetection performance and high flexibility even after bending and twisting approximately 300 cycles. The solid-state PEC-type $NbSe_2/Nb_2O_5$ photodetector was also assembled

by a solid electrolyte and flexible ITO-coated PET substrate and this photodetector also shows relatively stable photodetection. These results demonstrated that the 2D $NbSe_2/Nb_2O_5$ heterostructure has great potential in flexible optoelectronic devices.

Experimental section

In this work, 2D $NbSe_2$ nanosheets were easily exfoliated from bulk counterparts by using sonication-assisted exfoliation in 40% aqueous ethanol solution. 400 mg $NbSe_2$ powder was bath sonicated in 400 mL solvent by using a Qsonica Q700 supersonic machine for a total of 480 minutes. In order to introduce a size-dependent surface oxidation layer, the suspensions were then centrifuged at 1000, 3000, 5000, and 7000 rotation per minute (rpm) for 10 minutes, respectively. Each dispersion was then collected by pipet and deposited onto a flexible ITO-coated PET substrate by the electrophoretic deposition technique (Fig. 1a). The deposition time parameter was approximately 180 s at 90 V.

The fabricated flexible $NbSe_2/Nb_2O_5$-based PEC photodetectors were investigated in 1 M Na_2SO_4 electrolyte. Beyond that, the solid-state PEC photodetector was assembled by $NbSe_2/Nb_2O_5$ nanosheets, PET-ITO covered with carbon as a counter electrode, and black solid-state electrolyte (Fig. 1a). The real photos of the PEC photodetector and solid-state PEC photodetector can be found in Fig. 1a. These two types of PEC photodetectors were measured based on an electrochemical system,
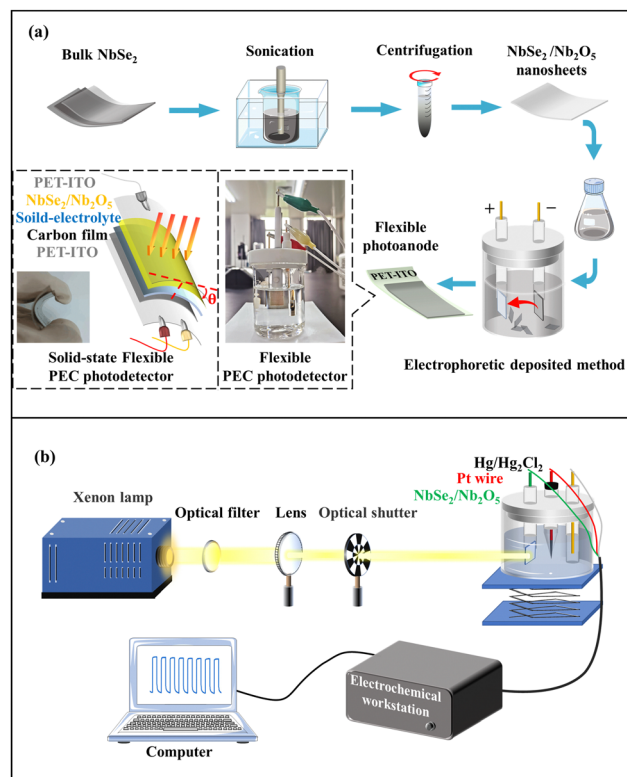

Fig. 1 (a) The preparation of the $NbSe_2/Nb_2O_5$-based PEC photodetector and solid-state PEC photodetector, and (b) photoelectric performance measurement.

which can work at different power intensities and wavelengths (Fig. 1b). In the PEC-type photodetector, the working electrode is PET-ITO covered with $NbSe_2/Nb_2O_5$ nanosheets, and the reference electrode is a Hg/Hg_2Cl_2 electrode while the counter electrode is Pt wire. In contrast, the counter and reference electrodes were both clamped on the same end of PET-ITO while the working electrode was clamped on PET-ITO covered with carbon and 2D $NbSe_2/Nb_2O_5$ films in the solid-state PEC photodetector.

Results and discussion

Transmission electron microscopy (TEM) was used to verify the successful exfoliation of size-dependent $NbSe_2$ nanosheets from bulk structures under different centrifugation speeds (Fig. 2a–d). The results show that the nanosheet size decreases from 350 to 50 nm in length and from 300 to 25 nm in width. The size and thickness information of the $NbSe_2$ nanosheet under the centrifugation speed of 5000 rpm are also characterized by scanning electron microscopy, as shown in Fig. S1 in the ESI.† The results show that the thickness of the $NbSe_2/Nb_2O_5$ film is 367.76 nm, which is stacked by nanosheets 113 nm in length and 90 nm in width. The results are in line with the TEM results in Fig. 2.

To confirm the size-dependent surface oxidation, atomic force microscopy (AFM) was used, as shown in Fig. 3. The results show that the average thicknesses of the nanosheets under different centrifugation speeds are 133.94, 76.72, 18.78, and 16.49 nm, respectively. In the ultrasonic stripping process, the surface oxide layer with the same thickness was introduced, but the whole thickness of $NbSe_2/Nb_2O_5$ shows a dramatic difference, thus leading to size-dependent surface oxidation. The results agree well with the XPS results, as shown in Fig. 4.

To verify the sample overall composition and crystalline structure, XRD measurements were performed (Fig. S2a) (ESI†).
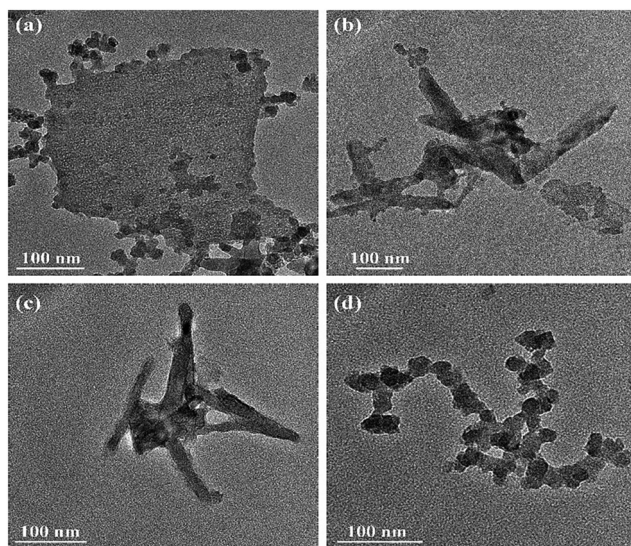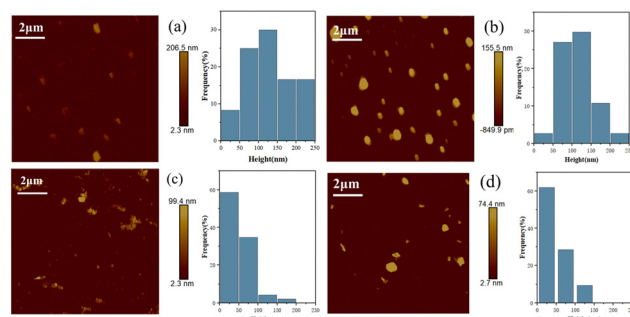

Fig. 3 AFM images and statistical size distribution of few-layer $NbSe_2/Nb_2O_5$ nanosheets under the centrifugation speed of (a) 1000 rpm, (b) 3000 rpm, (c) 5000 rpm, and (d) 7000 rpm.

The bulk powder and exfoliated nanosheets of $NbSe_2$ were characterized. Two obvious peaks at 14.26 and $43.49°$ correspond to (0 0 4) and (0 0 6) planes, indicating the successful preparation of $NbSe_2$ nanosheets.[36] However, there is a tiny peak at $9.66°$ in the exfoliated nanosheets, suggesting a thin surface oxidation (Nb_2O_5) layer. The thin surface functionalities of $NbSe_2$ are effectively characterized by XPS. The Se 3d spectrum (Fig. 4a) fitted by Se $3d_{5/2}$ (53.5 and 54.8 eV) and Se $3d_{3/2}$ (55.3 eV) agrees well with $NbSe_2$.[37] However, there is a small peak at 59.3 eV from Se 3d, suggesting the presence of selenium oxides. The peaks[27] at 531.6 and 530.1 eV (Fig. 4b) belong to O 1s and Nb_2O_5, respectively. Furthermore, the Nb 3d peaks (Fig. 4c) fitted by Nb $3d_{5/2}$ and Nb $3d_{3/2}$ locate at 206.9 and 209.5 eV. The peaks correspond to the Nb^{4+} and Nb^{5+}, indicating the presence of $NbSe_2$ and Nb_2O_5,[28] respectively. The results suggest that the bulk $NbSe_2$ powder has been partly oxidized at the surface. After the $NbSe_2$ nanosheets exfoliated from the bulk powder, the XPS spectra of Se 3d, O 1, and Nb 3d (Fig. 4d–f) were also fitted and these results show the increased amount of Nb_2O_5. After the formation of the $Nb_2O_5/NbSe_2$ heterostructure, the binding energy of the O 1s peak has a relative shift towards higher binding energy. These shifts can be explained by the efficient charge transfer from Nb_2O_5 to Nb_2Se_5, which is also found in 2D Bi_2S_3/ReS_2,[38] $SnSe_2/SnSe$[39] and $SnS/SnSe_2$[40] heterostructures.

Benefiting from the gradient centrifugation method, size-dependent surface oxidation of $NbSe_2$ photoanodes was performed on a flexible PET substrate. The photoelectric properties were firstly investigated under simulated sunlight illumination at 100 mW cm^{-2} and the I–V curve showed an obvious photovoltaic activity (Fig. S3a) (ESI†). It is known that the photodetectors are sensitive to external bias voltage. To evaluate the photoresponse of the $NbSe_2/Nb_2O_5$ based PEC-type photodetector under the different centrifugal speeds, time-dependent photocurrent density was measured at 0.2, 0.4, and 0.6 V (Fig. 5a–c), respectively. The steep rise and fall steps demonstrate a fast generation and separation of electron–hole pairs in the different size photodetector devices. Furthermore, all devices show an excellent reproducibility and stability to the on/off state approximately for 10 s per cycle. The photocurrent density ($I_{ph} = I_{on} - I_{off}$) and responsivity ($R_{ph} = I_{ph}/P$) parameters
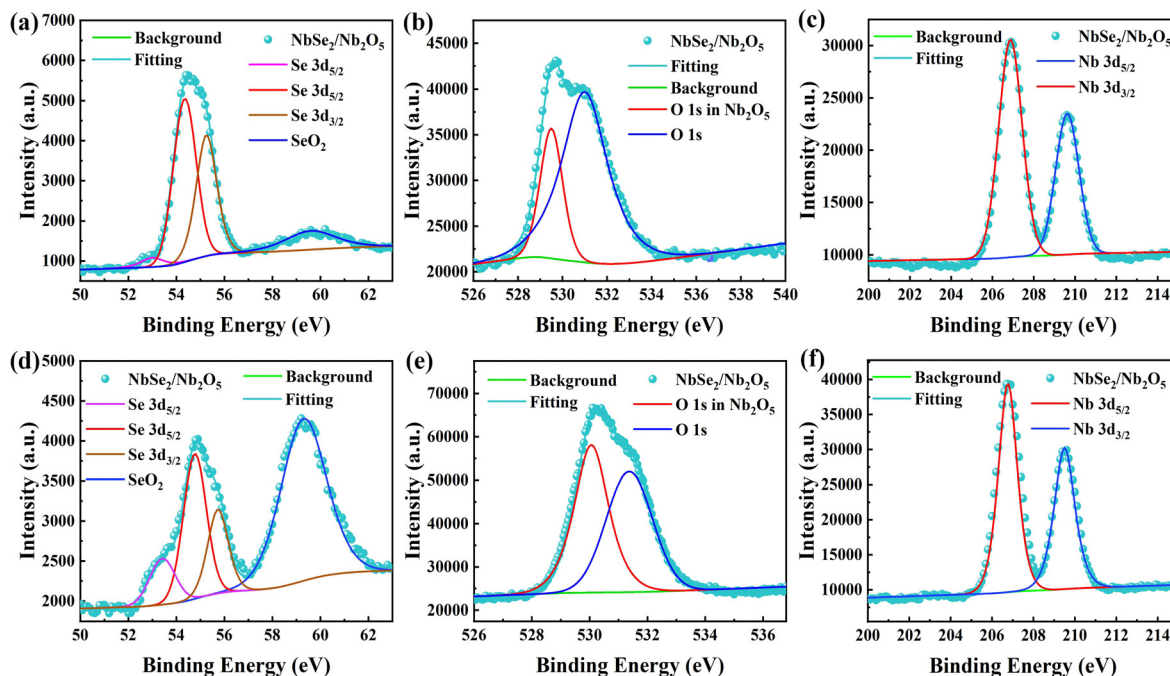

Fig. 2 TEM images of $NbSe_2$ nanosheets under the centrifugation speed of (a) 1000 rpm, (b) 3000 rpm, (c) 5000 rpm, and (d) 7000 rpm.

Fig. 4 XPS signal of bulk $NbSe_2$ with (a) Se, (b) O, and (c) Nb elements; XPS signal of $NbSe_2/Nb_2O_5$ nanosheets with (d) Se, (e) O, and (f) Nb elements.
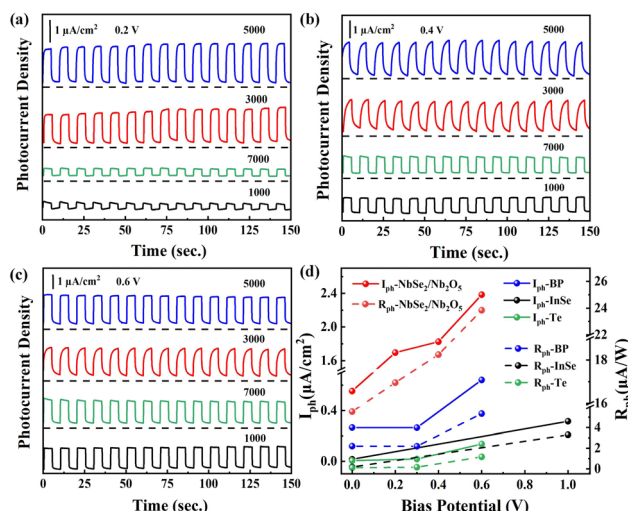

Fig. 5 Time-dependent photocurrent density of $NbSe_2/Nb_2O_5$ under the different centrifugal speed (1000, 3000, 5000, and 7000 rpm)-based PEC photodetectors was measured at (a) 0.2 V, (b) 0.4 V, and (c) 0.6 V; (d) I_{ph} and R_{ph} values of the 2D material-based PEC-type photodetector, including $NbSe_2/Nb_2O_5$ (this work), BP,[41] InSe,[43] and Te.[42]

are commonly used to assess photodetector performance. The detailed I_{ph} and R_{ph} values of different layers of $NbSe_2/Nb_2O_5$ photodetectors were measured, as shown in Fig. 5. It is noticeable that the I_{ph} and R_{ph} values of $NbSe_2/Nb_2O_5$ with different layers all increase with the external bias voltage due to the faster carrier separation under stronger electric fields, as shown in Fig. 5a–c. Among them, especially for the $NbSe_2/Nb_2O_5$ nanosheet deposited photodetector at 5000 rpm, the I_{ph} values

are 0.55, 1.69, 1.46, and 2.32 µA cm^{-2} and R_{ph} reaches 5.54, 16.95, 14.62, and 23.21 µA W^{-1} at 0, 0.2, 0.4, and 0.6 V, respectively. Even without external voltage (Fig. S3b) (ESI†), the $NbSe_2$ photodetector still can work due to the built-in electric field at the $NbSe_2/Nb_2O_5$ interface. These $NbSe_2/Nb_2O_5$ MSHS-based photodetectors all exhibit more superior photoelectric response in I_{ph} and R_{ph} than those of previously studied BP,[41] Te,[42] and InSe[43] based PEC-type photodetectors (Fig. 5d). This excellent photoelectric response of $NbSe_2$ may origin from the formation of a heterostructure interface between surface oxidation and metallic $NbSe_2$ behavior. The heterostructure prolongs the photoexcited carrier recombination and the metallic behavior of $NbSe_2$ accelerates the charge transfer process. In detail, the carrier separation and transfer pathways at the interface of $NbSe_2/Nb_2O_5$ are shown in Fig. S4 (ESI†).

To figure out the performance of the photoelectric response, the carrier transportation efficiency was investigated by electrochemical impedance spectrum (EIS) (Fig. 6a). The smaller semicircle suggests the lower interfacial resistance between the $NbSe_2/Nb_2O_5$ photoanode and the electrolyte, benefiting carrier separation and transportation. Beyond that, the carrier transportation efficiency can directly reflect from the characteristic peak frequency in Bode phase plots (Fig. 6b). The results demonstrate that the lower frequency of the 5000 rpm nanosheet-coated $NbSe_2/Nb_2O_5$ film reaches 0.68 Hz, suggesting fast electron transfer. This outstanding carrier separation and recombination property indicates higher response speed. Here, we mainly study the photoelectric performance of the $NbSe_2/Nb_2O_5$-based photodetector at 5000 rpm. In this work, the response time is characterized by using an optical chopper to generate pulsed light at 1000 Hz (Fig. 6c). From the enlarged
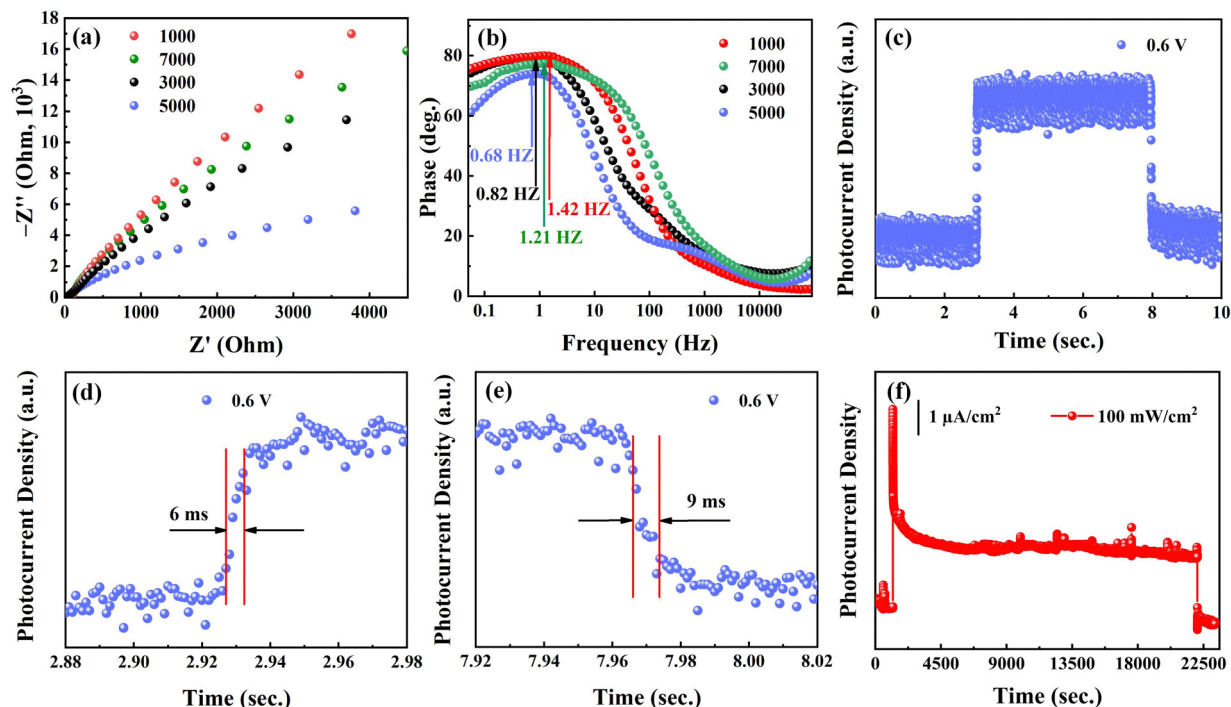
Fig. 6 (a) EIS spectra, (b) Bode plots of NbSe$_2$/Nb$_2$O$_5$ photoelectrodes covered with different sizes of nanosheets, (c) response time including (d) rise time (t_r) and (e) fall time (t_f), and (f) long-term stability measurement.

rise and fall step (Fig. 6d and e), the rise time (t_r) and fall time (t_f) are 6 ms and 9 ms at 0.6 V, indicating high sensitivity. The fall time is longer than the rise time, indicating defect states and charge carrier traps in the 2D NbSe$_2$/Nb$_2$O$_5$ materials.[44] It is worth pointing out that the response time is 1−2 orders of magnitude faster than previous reported 2D PEC-type photodetectors such as SnS,[45] Te,[42] InSe,[43] Bi$_2$S$_3$,[46] and BP[41] (Table 1). Despite the lower responsivity in the NbSe$_2$/Nb$_2$O$_5$, such response speed is far superior to FET-type photodetectors such as GeS,[47] SnS$_2$,[48] and MoS$_2$[49] due to high electrical conductivity, reduced contact resistance and Schottky barrier.[19,20] The high sensitivity promises the NbSe$_2$/Nb$_2$O$_5$ MSHS as a promising alternative for the photodetector, particularly for optical communication and imaging.

Apart from the sensitivity, the stability of the device is also one of the key performance indicators of commercial photodetectors. The long-term stability tests of the NbSe$_2$/Nb$_2$O$_5$-based photodetector are measured about 23300 s with the applied potential at 0.6 V (Fig. 6f). It can be found that the I_{ph}

can still be maintained at a relatively high level (2.10 μA cm^{-2}) even though the photodetector was located in 1 M Na$_2$SO$_4$ electrolyte. However, when we characterize the stability by long cycle measurement under on/off state (Fig. 7a), the I_{ph} gradually increases from 2.0 μA cm^{-2} to 5.13 μA cm^{-2} within 19950 s under the same irradiation intensity of 100 mW cm^{-2}. The sharp peak may be from the large amount of electron accumulation and fast recombination. Along with the time variation, the gradually increased I_{ph} may be due to the oxygen-sensitized photoconduction (OSPC) mechanism, which is frequently observed in ZnO,[50] WO$_3$,[44] and TiO$_2$.[51] Furthermore, the surface oxidation has been demonstrated by XPS and this mechanism is mainly dominated by the surface. Based on the OSCP model, there are four main processes (Fig. 7b). (i) Under the dark state, the oxygen molecule is absorbed on the surface of Nb$_2$O$_5$ and acts as an electron capture center [O$_2$(g) + e$^-$ → O$_2^-$(ad)], thus leading to the surface band bending. (ii) Under the light illumination state, when the photon energy is above the band gap, electron-hole pairs are generated

Table 1 NbSe$_2$/Nb$_2$O$_5$ nanosheet-based photodetector with other reported photoanodes

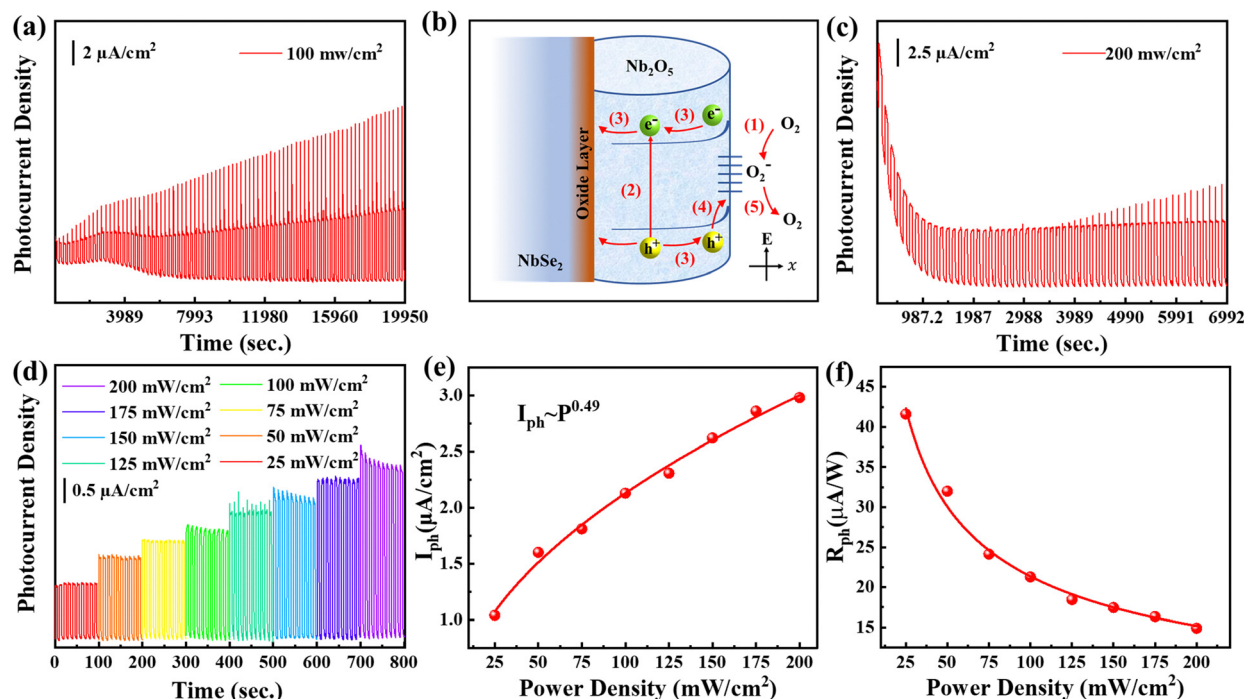| Materials	Measurement conditions	Response time	Responsivity	Ref.
NbSe$_2$/Nb$_2$O$_5$	0.1 M Na$_2$SO$_4$, 0.6 V	6 ms	23.84 μA W^{-1}	This work
SnS	0.1 M Na$_2$SO$_4$, 0.6 V	0.3 s	17.8 μA W^{-1}	45
Te	0.1 M Na$_2$SO$_4$, 0.6 V	70 ms	1.0–1.3 μA W^{-1}	42
InSe	0.2 M KOH, 1 V	5 s	3.3 μA W^{-1}	43
Bi$_2$S$_3$	0.1 M KOH, 0.6 V	0.1 s	52 μA W^{-1}	46
BP	0.1 M KOH, 0 V	0.5 s	1.9–2.2 μA W^{-1}	41
GeS	FET, 500 nm, V_{ds} = 5 V	0.85 s	139.9 μA W^{-1}	47
SnS$_2$	FET, 450 nm, V_{ds} = 10 V	42 ms	2 A W^{-1}	48
MoS$_2$	Schottky-contact, V_{ds} = 5 V	4 s	880 A W^{-1}	49

Fig. 7 (a) Long cycling stability measurement in a low oxygen environment, (b) OSPC mechanism, (c) long cycling stability measurement in enough oxygen environment, (d) light intensity-dependent photocurrent density, and (e) I_{ph} and (f) R_{ph} values extracted from (d).

$(h\nu = e^- + h^+)$. (iii) Subsequently, the electron-hole pairs are separated by surface band bending and holes flow to the surface while electrons transit from the valence band to the conduction band. (iv) The holes act with the negatively charged oxygen ions, which then release an oxygen molecule $[O_2^-(ad) + h^+ \rightarrow O_2(g)]$. As the holes are consumed, the unpaired electrons would be captured in the process (i), thus resulting in a longer lifetime and higher photocurrent. Furthermore, the low oxygen content in the electrolyte and lower oxygen adsorption rate would lead to higher I_{ph} with the time variation. After the test is finished, the NbSe$_2$/Nb$_2$O$_5$ was further characterized by XPS (Fig. S5a–c) (ESI†). The results show that the surface oxidation gradually increases, suggesting that the oxygen is consumed and the oxygen adsorption takes place. To verify the oxygen adsorption and desorption process, the oxygen purges electrolyte and promises more oxygen dissolved into the electrolyte. The XPS results (Fig. S5d–f) (ESI†) confirm that the surface NbSe$_2$ has been almost fully oxidized and the oxygen is enough. It is interesting to find that the stable long cycle on/off photocurrent density is approximately 2.98 μA cm^{-2} even under 200 mW cm^{-2} (Fig. 7c). These results demonstrated the OSCP takes place due to the surface oxidation.

The surface defects can also be characterized by light intensity photocurrent density, as shown in Fig. 7d. The intensity-dependent I_{ph} and R_{ph} values are extracted (Fig. 7e and f). The I_{ph} curves (Fig. 7e) are fitted by power law ($I_{ph} \sim p^\theta$), and the fitted θ is 0.49 smaller than 1,[52,53] indicating the presence of some trap states in the NbSe$_2$ surface. The R_{ph} value (Fig. 7f) decreases with light intensity due to the trap states. Under low light intensity, the photoexcited electrons would be captured by trap states, resulting in reduced recombination.[54]

Correspondingly, the carrier lifetime is largely prolonged, giving rise to higher R_{ph}. Under high light intensity, the trap states are quickly filled,[55] eventually leading to the saturation of R_{ph}.

To fully assess the photodetection performance of the NbSe$_2$/Nb$_2$O$_5$ based PEC-type photodetector, the photoelectric response is characterized at the wavelengths of 380, 420, 450, 475, 500, 520, 550, 600, and 650 nm (Fig. 8a). The NbSe$_2$/Nb$_2$O$_5$ shows a higher photoresponsivity at 380 nm, and the value reaches 23.84 μA W^{-1}, which is larger than those of 2D materials such as SnS/SnSe$_2$,[40] Te/Se,[56] and Nb$_2$C.[31] We also extract the I_{ph} and R_{ph} (Fig. 8b) and these values gradually decrease with the wavelength due to the decreased photon absorption as depicted in the UV-Vis spectra (Fig. S2b in ESI†). According to the above-calculated R_{ph}, specific detectivity (D^*) is defined and calculated by $D^* = R \times S^{1/2}/(2 \times q \times I_{off})^{1/2}$, where q and S are 1.60×10^{-19} C and 0.6 cm^2. The calculated D^* value is summarized (Fig. 8c) and the maximum D^* value is 7.03×10^8 Jones in 380 nm and the reduced D^* with wavelength is due to the high UV response of Nb$_2$O$_5$.[26]

To further test the flexibility performance of the NbSe$_2$/Nb$_2$O$_5$ PEC photodetector, the photoanode was bent approximately at 0, 100, 200, and 300 cycles. The photos of the photodetectors under 0, 100, 200, and 300 cycles can be found in Fig. S6 in the ESI.† The stable photoelectric response is shown in Fig. 8d and the I_{ph} keeps approximately 2.32 μA cm^{-2}, indicating the excellent flexibility performance. Beyond that, the photoresponse was also measured (Fig. 8e) at different bending angles including 0, 15, 45, 60, and 75° and the I_{ph} almost remains the same, which further indicates the NbSe$_2$/Nb$_2$O$_5$
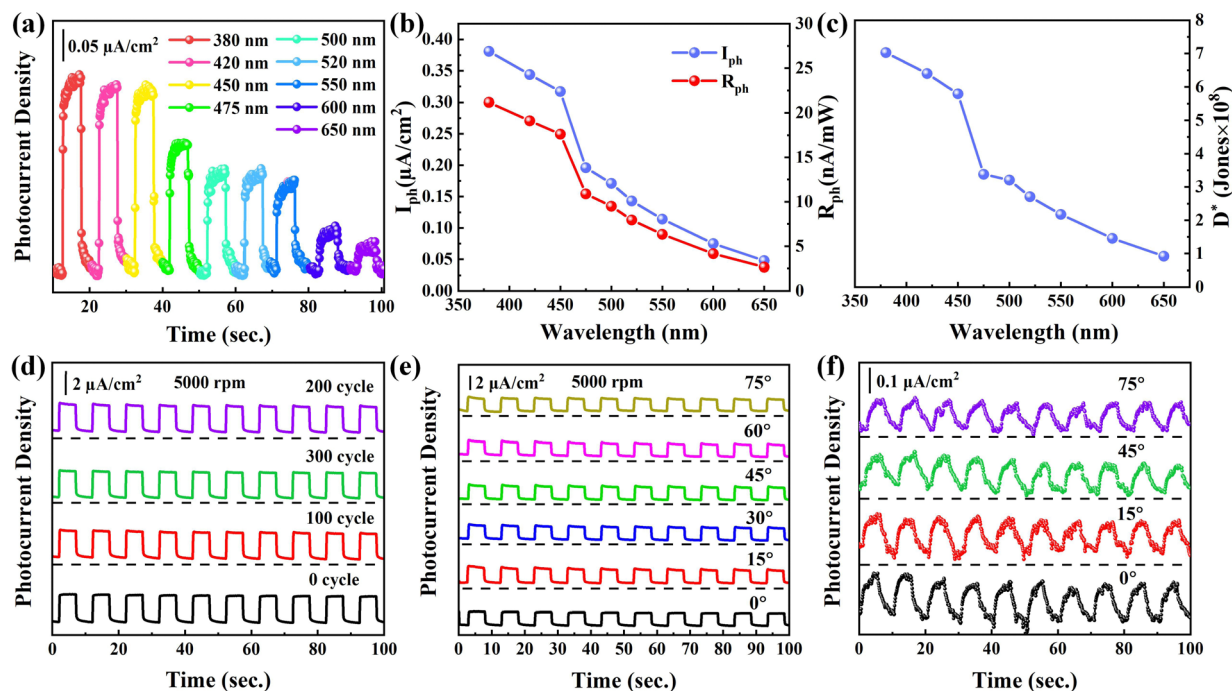
Fig. 8 (a) Photocurrent density, (b) the calculated I_{ph} and R_{ph}, and (c) specific detectivity (D^*) values under different wavelengths; flexibility measurement with (d) different bending cycles and (e) bending angles in the PEC-type photodetector; (f) flexibility measurement in various bending angles in a solid photodetector.

Table 2   Performance comparison of PEC-type photodetectors

Materials	Measurement conditions	Response time	Responsivity	Flexible?	Ref.
$NbSe_2/Nb_2O_5$	0.1 M Na_2SO_4, 0.6 V	6 ms	23.84 μA W^{-1}	Yes	This work
MoS_2/WS_2	FET, 405 nm, Vds = 6 V	9 ms	298 A W^{-1}	No	58
ZnS/MoS_2	ohmic contact, 554 nm,	11 s	17.85 μA W^{-1}	Yes	59
Graphene/ZnO	Schottky-contact, Vds = 0 V	32 ms	50 μA W^{-1}	No	60
$SnS/SnSe_2$	0.5 M Na_2SO_4, 0.6 V	29.6 ms	4.76 μA W^{-1}	No	40
Te/Se	1.0 M KOH, 0 V	2 s	4.04 μA W^{-1}	No	41
Bi/Te	0.5 M KOH, 0 V	20 ms	67.67 μA W^{-1}	No	61
Bi_2O_2Se/graphene	KOH/PVA (Quasi-solid)	0.4 s	6.5 μA W^{-1}	Yes	57
WS_2/graphene	H_2SO_4/PVA (Quasi-solid)	1.2 s	36 mA W^{-1}	Yes	62

PEC-photodetector with good flexibility. To meet the commercial applications, the solid-state PEC photodetector is greatly anticipated and then the sandwich-structure $NbSe_2/Nb_2O_5$ photodetector is fabricated, where the aqueous solution is replaced by a solid electrolyte as a charge transfer medium. An obvious on/off photocurrent density signal was observed and the I_{ph} value reaches 0.13 μA cm^{-2} (Fig. 8f). Even though the solid-state PEC photodetector performance is slightly lower than that of the PEC-type photodetector in the liquid electrolyte, the photocurrent density of the solid device shows no obvious changes even at 15, 45, and 75° after being bent, implying superior flexibility. Compared with the state-of-the-art reports, such as $SnS/SnSe_2$,[40] Te/Se,[56] and Bi_2O_2Se/Graphene[57] in Table 2, the excellent photodetection performance suggests the further utilization of the $NbSe_2/Nb_2O_5$ photodetector in highly sensitive, flexible, and wearable optoelectronic devices.

Conclusions

In summary, size-dependent $NbSe_2/Nb_2O_5$ MSHSs were successfully prepared and applied to PEC-type photodetectors. This photodetector shows excellent photodetection performance such as high responsivity ($\sim$23.21 μA W^{-1}), fast response speed at the millisecond level, and broad band detection in the UV-Vis region. It is interesting to find that the I_{ph} is dependent on the ambient environment due to oxygen-sensitized photoconduction. Beyond that, the $NbSe_2/Nb_2O_5$ MSHS-based PEC-type photodetector still exhibits high photodetection performance and high flexibility even after bending and twisting approximately 300 cycles. The solid-state PEC-type $NbSe_2/Nb_2O_5$ MSHS photodetector also shows relatively stable photodetection. This work demonstrated that 2D metal-semiconductor heterostructures have great potential in a high-performance optoelectronic device.

Author contributions

Xiang Xu: project administration, writing – review and editing & funding acquisition; Chunhui Lu: writing – review and editing, conceptualization; Ying Wang: writing – original draft, formal analysis; Xing Bai: conceptualization & data curation; Zenghui Liu: visualization; Ying Zhang: formal analysis; Dengxin Hua: supervision.

Conflicts of interest

The authors declare that they have no known competing financial interests or personal relationships that could have appeared to influence the work reported in this paper.

Acknowledgements

Notes and references

1 Q. H. Wang, K. Kalantar-Zadeh, A. Kis, J. N. Coleman and M. S. Strano, *Nat. Nanotechnol.*, 2012, **7**, 699–712.

2 X. Yu, M. S. Prevot, N. Guijarro and K. Sivula, *Nat. Commun.*, 2015, **6**, 7596.

3 K. F. Mak, C. Lee, J. Hone, J. Shan and T. F. Heinz, *Phys. Rev. Lett.*, 2010, **105**, 136805.

4 M. Bernardi, M. Palummo and J. C. Grossman, *Nano Lett.*, 2013, **13**, 3664–3670.

5 R. Tenne and A. Wold, *Appl. Phys. Lett.*, 1985, **47**, 707–709.

6 J. Chen, W. Ouyang, W. Yang, J. H. He and X. Fang, *Adv. Funct. Mater.*, 2020, 30.

7 W. Ouyang, F. Teng, J. H. He and X. Fang, *Adv. Funct. Mater.*, 2019, 29.

8 X. Fang, L. Hu, K. Huo, B. Gao, L. Zhao, M. Liao, P. K. Chu, Y. Bando and D. Golberg, *Adv. Funct. Mater.*, 2011, **21**, 3907–3915.

9 Z. Zhang, Y. Ning and X. Fang, *J. Mater. Chem. C*, 2019, **7**, 223–229.

10 W. Song, J. Chen, Z. Li and X. Fang, *Adv. Mater.*, 2021, **33**, 2101059.

11 M. S. El-Bana, D. Wolverson, S. Russo, G. Balakrishnan, D. M. Paul and S. J. Bending, *Supercond. Sci. Technol.*, 2013, **26**, 125020.

12 J. Li, P. Song, J. Zhao, K. Vaklinova, X. Zhao, Z. Li, Z. Qiu, Z. Wang, L. Lin, M. Zhao, T. S. Herng, Y. Zuo, W. Jonhson, W. Yu, X. Hai, P. Lyu, H. Xu, H. Yang, C. Chen, S. J. Pennycook, J. Ding, J. Teng, A. H. Castro Neto, K. S. Novoselov and J. Lu, *Nat. Mater.*, 2021, **20**, 181–187.

13 C. S. Lian, C. Si and W. Duan, *Nano Lett.*, 2018, **18**, 2924–2929.

14 S. K. Bae, H. K. Kim, Y. B. Lee, X. F. Xu and S. Iijima, *Nat. Nanotechnol.*, 2011, **5**, 574–578.

15 H. G. Shin, H. S. Yoon, J. S. Kim, M. Kim, J. Y. Lim, S. Yu, J. H. Park, Y. Yi, T. Kim and S. C. Jun, *Nano Lett.*, 2018, **18**, 1937–1945.

16 R. Corcoran, P. Meeson, Y. Onuki, P. A. Probst and B. L. Gyorffy, *J. Phys.: Condens. Matter*, 1994, **6**, 4479–4492.

17 J. Tan, S. Li, B. Liu and H. M. Cheng, *Small Struct.*, 2021, **2**, 2000093.

18 Y. Zhang, L. Yin, J. Chu, T. A. Shifa, J. Xia, F. Wang, Y. Wen, X. Zhan and H. Jun, *Adv. Mater.*, 2018, **30**, 1803665.

19 V. T. Vu, T. Vu, T. L. Phan, W. T. Kang, Y. R. Kim, M. Tran, H. Nguyen, Y. H. Lee and W. J. Yu, *ACS Nano*, 2021, **15**, 13031–13040.

20 D. M. Seo, J. H. Lee, S. Lee, J. Seo and M. G. Hahm, *ACS Photonics*, 2019, **6**, 1379–1386.

21 N. Guijarro, M. S. Prevot and K. Sivula, *Phys. Chem. Chem. Phys.*, 2015, **17**, 15655–15674.

22 Y.-R. Chang, P.-H. Ho, C.-Y. Wen, T.-P. Chen, S.-S. Li, J.-Y. Wang, M.-K. Li, C.-A. Tsai, R. Sankar, W.-H. Wang, P.-W. Chiu, F.-C. Chou and C.-W. Chen, *ACS Photonics*, 2017, **4**, 2930–2936.

23 M. Yamamoto, S. Dutta, S. Aikawa, S. Nakaharai, K. Wakabayashi, M. S. Fuhrer, K. Ueno and K. Tsukagoshi, *Nano Lett.*, 2015, **15**, 2067–2073.

24 Y. Wang, A. Chen, S. Lai, X. Peng, S. Zhao, G. Hu, Y. Qiu, J. Ren, X. Liu and J. Luo, *J. Catal.*, 2020, **381**, 78–83.

25 A. Le Viet, R. Jose, M. V. Reddy, B. V. R. Chowdari and S. Ramakrishna, *J. Phys. Chem. C*, 2010, **114**, 21795–21800.

26 R. Ghosh, M. K. Brennaman, T. Uher, M.-R. Ok, E. T. Samulski, L. E. McNeil, T. J. Meyer and R. Lopez, *ACS Appl. Mater. Interfaces*, 2011, **3**, 3929–3935.

27 R. Qu, X. Wen, Y. Zhao, T. Wang, R. Yao and J. Lu, *Ultrason. Sonochem.*, 2021, **73**, 105491.

28 H. M. N. Ahmad, S. Ghosh, G. Dutta, A. G. Maddaus, J. G. Tsavalas, S. Hollen and E. Song, *J. Phys. Chem. C*, 2019, **123**, 8671–8680.

29 K. Wang, Y. Feng, C. Chang, J. Zhan, C. Wang, Q. Zhao, J. N. Coleman, L. Zhang, W. J. Blau and J. Wang, *Nanoscale*, 2014, **6**, 10530–10535.

30 C. Lu, D. Yang, J. Ma, M. Luo, Y. Jin and X. Xu, *Appl. Surf. Sci.*, 2020, **532**, 147409.

31 L. Gao, C. Ma, S. Wei, A. V. Kuklin, H. Zhang and H. Agren, *ACS Nano*, 2021, **15**, 954–965.

32 Z. Guo, R. Cao, H. Wang, X. Zhang, F. Meng, X. Chen, S. Gao, D. K. Sang, T. H. Nguyen, A. T. Duong, J. Zhao, Y. J. Zeng, S. Cho, B. Zhao, P. H. Tan, H. Zhang and D. Fan, *Natl. Sci. Rev.*, 2022, **9**, nwab098.

33 H. Qiao, Z. Huang, X. Ren, S. Liu, Y. Zhang, X. Qi and H. Zhang, *Adv. Opt. Mater.*, 2019, **8**, 1900765.

34 T. Fan, Z. Xie, W. Huang, Z. Li and H. Zhang, *Nanotechnology*, 2019, **30**, 114002.

35 Y. Zhang, P. Huang, J. Guo, R. Shi, W. Huang, Z. Shi, L. Wu, F. Zhang, L. Gao, C. Li, X. Zhang, J. Xu and H. Zhang, *Adv. Mater.*, 2020, **32**, e2001082.

36 N. D. Boscher, C. J. Carmalt and I. P. Parkin, *Eur. J. Inorg. Chem.*, 2006, 1255–1259.

37 H. Wang, X. Huang, J. Lin, J. Cui, Y. Chen, C. Zhu, F. Liu, Q. Zeng, J. Zhou, P. Yu, X. Wang, H. He, S. H. Tsang, W. Gao,

K. Suenaga, F. Ma, C. Yang, L. Lu, T. Yu, E. H. T. Teo, G. Liu and Z. Liu, *Nat. Commun.*, 2017, **8**, 394.

38 C. Lu, M. Luo, D. Yang, J. Ma, M. Qi and X. Xu, *Adv. Mater. Interfaces*, 2021, **8**, 2100913.

39 C. Lu, W. Dong, Y. Zou, Z. Wang, J. Tan, X. Bai, N. Ma, Y. Ge, Q. Zhao and X. Xu, *ACS Appl. Mater. Interfaces*, 2023, **15**, 6156–6168.

40 W. Dong, C. Lu, M. Luo, Y. Liu, T. Han, Y. Ge, X. Xue, Y. Zhou and X. Xu, *J. Colloid Interface Sci.*, 2022, **621**, 374–384.

41 X. Ren, Z. Li, Z. Huang, D. Sang, H. Qiao, X. Qi, J. Li, J. Zhong and H. Zhang, *Adv. Funct. Mater.*, 2017, **27**, 1606834.

42 Z. Xie, C. Xing, W. Huang, T. Fan, Z. Li, J. Zhao, Y. Xiang, Z. Guo, J. Li, Z. Yang, B. Dong, J. Qu, D. Fan and H. Zhang, *Adv. Funct. Mater.*, 2018, **28**, 1705833.

43 Z. Li, H. Qiao, Z. Guo, X. Ren, Z. Huang, X. Qi, S. C. Dhanabalan, J. S. Ponraj, D. Zhang, J. Li, J. Zhao, J. Zhong and H. Zhang, *Adv. Funct. Mater.*, 2018, **28**, 1705237.

44 K. Huang, Q. Zhang, F. Yang and D. He, *Nano Res.*, 2010, **3**, 281–287.

45 W. Huang, Z. Xie, T. Fan, J. Li, Y. Wang, L. Wu, D. Ma, Z. Li, Y. Ge, Z. N. Huang, X. Dai, Y. Xiang, J. Li, X. Zhu and H. Zhang, *J. Mater. Chem. C*, 2018, **6**, 9582–9593.

46 W. Huang, C. Xing and Y. Wang, *et al.*, *Nanoscale*, 2018, **10**, 2404–2412.

47 C. Y. Lan, C. Li, Y. Yin, H. Y. Guo and S. Wang, *J. Mater. Chem. C*, 2015, **3**, 8074–8079.

48 J. Xia, D. Zhu, L. Wang, B. Huang, X. Huang and X. M. Meng, *Adv. Funct. Mater.*, 2015, **25**, 4255–4261.

49 O. Lopez-Sanchez, D. Lembke, M. Kayci, A. Radenovic and A. Kis, *Nat. Nanotechnol.*, 2013, **8**, 497–501.

50 C. Soci, A. Zhang, B. Xiang, S. A. Dayeh, D. P. R. Aplin, J. Park, X. Y. Bao, Y. H. Lo and D. Wang, *Nano Lett.*, 2007, **7**, 1003–1009.

51 R. S. Chen, C. A. Chen, H. Y. Tsai, W. C. Wang and Y. S. Huang, *J. Phys. Chem. C*, 2012, **116**, 4267–4272.

52 L. H. Zeng, M. Z. Wang, H. Hu, B. Nie, Y. Q. Yu, C. Y. Wu, L. Wang, J. G. Hu, C. Xie, F. X. Liang and L. B. Luo, *ACS Appl. Mater. Interfaces*, 2013, **5**, 9362–9366.

53 L. Li, E. Auer, M. Liao, X. Fang, T. Zhai, U. K. Gautam, A. Lugstein, Y. Koide, Y. Bando and D. Golberg, *Nanoscale*, 2011, **3**, 1120–1126.

54 L. Wang, J. Jie, Z. Shao, Q. Zhang, X. Zhang, Y. Wang, Z. Sun and S.-T. Lee, *Adv. Funct. Mater.*, 2015, **25**, 2910–2919.

55 H. Xu, J. Wu, Q. Feng, N. Mao, C. Wang and J. Zhang, *Small*, 2014, **10**, 2300–2306.

56 Y. Wang, F. Zhao, Y. Wang, Y. Zhang, Y. Shen, Y. Feng and W. Feng, *Compos. Commun.*, 2022, 32.

57 G. Chen, Y. Zhou, G. Zhang, J. Li and X. Qi, *Ceram. Int.*, 2021, **47**, 25255–25263.

58 X. Lin, F. Wang, X. Shan, Y. Miao, X. Chen, M. Yan, L. Zhang, K. Liu, J. Luo and K. Zhang, *Appl. Surf. Sci.*, 2021, 546.

59 P. T. Gomathi, P. Sahatiya and S. Badhulika, *Adv. Funct. Mater.*, 2017, 27.

60 D. Chen, Y. Xin, B. Lu, X. Pan, J. Huang, H. He and Z. Ye, *Appl. Surf. Sci.*, 2020, 529.

61 Y. Zhang, J. Guo, J. Xu, W. Huang, C. Li, L. Gao, L. Wu, Z. Shi, C. Ma, Y. Ge, X. Zhang and H. Zhang, *Nanoscale Horiz.*, 2020, **5**, 847–856.

62 X. Ren, B. Wang, Z. Huang, H. Qiao, C. Duan, Y. Zhou, J. Zhong, Z. Wang and X. Qi, *FlatChem*, 2021, 25.